Traffic Light Detection Method for Underground CO_2 Injection–Induced Seismicity

Xiaochen Wei[1]; Qi Li[2]; Xiaying Li[3]; and Zhiyong Niu[4]

Abstract: Pressure buildup induced by geological carbon sequestration (GCS) will decrease the effective stresses in the storage formation, and geomechanical effects of overpressure may affect fault stability, possibly resulting in felt induced seismicity. Predicting the geomechanical stability of faults is of crucial importance for the safety of GCS. We applied a numerical approach to evaluate the potential magnitude of fault slippage for a specific stress regime. Next, we focused on the geometry and structures of fault zones through comprehensive analyses of the thickness of the overburden (H), the fault dip (Φ), and the distance between the fault and the injection well (D). Based on the relationships of D, H, and Φ with the corresponding fault behavior, we obtained a traffic light indicator diagram to assess the risk of induced seismicity at a specific level of each factor. To overcome the complicated relationship between factor variations and the corresponding fault slippage, we introduced a danger surface in the traffic light indicator diagram with a security threshold of inducing moderate to strong seismicity to distinguish the danger zone. This approach provides physically sound outcomes for prioritizing the well location to avoid the risk of inducing strong seismicity. **DOI: 10.1061/(ASCE)GM.1943-5622.0001573.**

Author keywords: Geological carbon sequestration; Fault stability; Induced seismicity; Traffic light detection method; Subsurface fluid injection.

Introduction

Geological carbon sequestration (GCS) is widely regarded as an effective approach for achieving large reductions in greenhouse gas emissions to alleviate climate change during the next several decades (IPCC 2005). According to the International Energy Agency (IEA), GCS has the potential to contribute to 20% of the total carbon emissions reduction (IEA 2006). Fully commercial GCS projects will require the geological sequestration of large volumes of carbon dioxide (CO_2) to effectively reduce greenhouse gas emissions (e.g., >20 Mt) (Gerstenberger et al. 2013). As a result of the pressure buildup arising from such huge amounts of CO_2 injection into the deep subsurface, GCS could cause stress changes sufficient to bring about the reactivation of pre-existing faults via seismicity over time (Mazzoldi et al. 2012; Zoback and Gorelick 2012).

In the context of GCS, the key issues for the reactivation of pre-existing faults are leakage of the trapped gas and induced seismicity (IPCC 2005; Lei et al. 2008; Li et al. 2013). Fault reactivation may increase the porosity and permeability of fault zones and thus provide leakage pathways into surrounding formations (Réveillère et al. 2012). However, CO_2 leakage is unlikely to occur because the heterogeneity of faults hinders the upward migration of CO_2 in the crystalline basement, where fault reactivation usually occurs (Vilarrasa et al. 2016; Li et al. 2004). More importantly, such human-induced seismicity accompanied by fault reactivation is a major environmental concern that may be felt by the local community and may put at risk successful project completion, because moderate to strong seismicity can cause damage to infrastructure or injury (Gerstenberger et al. 2013; Rutqvist et al. 2015). To date, several underground fluid injection projects have been halted because of induced seismicity, e.g., the enhanced geothermal system (EGS) project within the city of Basel in Switzerland (Häring et al. 2008) and the wastewater disposal projects at Guy, Arkansas (Horton 2012) and near Youngstown, Ohio (Ellsworth 2013). Faults are tectonic fractures that result in discontinuity in geological formations, across which relative displacements of adjacent layers have occurred (Childs et al. 1996; Vishal et al. 2015). The largest earthquakes associated with fluid injection and fluid retrieval operations often are induced by fault slippage (Gutierrez et al. 2000). The reactivation of faults during injection or depletion can be assessed using different approaches. Two commonly used methods for evaluating the potential reactivation of faults are analytical and numerical solutions (Gerstenberger et al. 2013). The reactivation of faults caused by injection or production is a complex problem that requires comprehensive analyses of initial and induced stresses versus the strength properties of the fault zone material. Some of these aspects can be captured by numerical modeling (Cappa and Rutqvist 2012; Gerstenberger et al. 2013; Rohmer et al. 2014; Rutqvist et al. 2013). Numerical and physical models that fully couple fluid flow within a porous

[1]Lecturer, School of Geoscience and Technology, Southwest Petroleum Univ., Chengdu 610500, China; State Key Laboratory of Geomechanics and Geotechnical Engineering, Institute of Rock and Soil Mechanics, Chinese Academy of Sciences, Wuhan 430071, China. Email: achencumt@163.com

[2]Professor, State Key Laboratory of Geomechanics and Geotechnical Engineering, Institute of Rock and Soil Mechanics, Chinese Academy of Sciences, Wuhan 430071, China; Univ. of Chinese Academy of Sciences, Beijing 100049, China (corresponding author). ORCID: https://orcid.org/0000-0003-0679-4385. Email: qli@whrsm.ac.cn

[3]Lecturer, State Key Laboratory of Geomechanics and Geotechnical Engineering, Institute of Rock and Soil Mechanics, Chinese Academy of Sciences, Wuhan 430071, China; Univ. of Chinese Academy of Sciences, Beijing 100049, China. Email: xyli@whrsm.ac.cn

[4]Lecturer, State Key Laboratory of Geomechanics and Geotechnical Engineering, Institute of Rock and Soil Mechanics, Chinese Academy of Sciences, Wuhan 430071, China; Univ. of Chinese Academy of Sciences, Beijing 100049, China. Email: niuzhiyong88@163.com

Note. This manuscript was submitted on February 8, 2019; approved on July 11, 2019; published online on December 5, 2019. Discussion period open until May 5, 2020; separate discussions must be submitted for individual papers. This paper is part of the ***International Journal of Geomechanics***, © ASCE, ISSN 1532-3641.

and fractured medium to the elastic behavior of the medium to account for nonlinearity effects can provide critical insight into the response of geological systems during fluid injection or depletion. For hydrocarbon applications, geomechanical modeling has been widely used to estimate reservoir compaction, surface subsidence, wellbore stability, and so forth (Zhou and Burbey 2014a; Zhu et al. 2015). Recently, this methodology has been extended to GCS to evaluate cap rock integrity or fault reactivation during CO_2 injection and storage (Rohmer et al. 2014; Shukla et al. 2011; Vidal-Gilbert et al. 2009; Wang et al. 2016).

Analytical approaches are powerful tools for a preliminary evaluation of the fault reactivation potential. They have been widely used in CO_2 storage, geothermal reservoirs, and waste disposal sites (Holloway 1997; Langhi et al. 2010). However, the analytical approach relies on many assumptions and simplifications, and thus has limitations in explaining real fault behavior during fluid injection or depletion. First, analytical approaches cannot consider a change of stress around faults. Some approaches can consider the change in the total stress magnitude. However, fluid injection or depletion changes not only the magnitude but also the direction of the principal stresses (Murphy et al. 2013; Rutqvist et al. 2007). This factor may introduce uncertainties in the estimated fault reactivation potential. Next, the slip tendency estimated using an analytical approach and the change in reservoir pressure can be applied only to the reservoir boundary; i.e., the calculated fault reactivation derived from an analytical approach may provide limited information on the slip tendency (Rice and Rudnicki 1979). Such analytical approaches may require additional validation.

The magnitude of induced earthquakes is a function of the fault rock mechanical properties and the size of the slip patch, which is affected by the pore-pressure buildup as well as the geometry, structures, and characteristics of fault zones (Koestler and Milnes 1992; Sabetamal et al. 2018; Li et al. 2006). Numerous studies have been conducted on the geometry, structures, and characteristics of fault zone properties over the last decades (Luther et al. 2013; Sylvester 1988). A fault zone typically consists of two substructures: the fault core, and the fault damage zone. A fault core generally comprises gouge and cataclasite, and damage surrounding the core of faults is represented by deformation over a range of scales from microfracturing of the rock matrix to macroscopic fracture networks (Mitchell and Faulkner 2009). The concentration of deformation adjacent to larger faults causes slippage in the damage zone, which is crucial for the hydromechanical behavior (Koestler and Milnes 1992; Yin et al. 2018). The assessment of injection-induced fault reactivation requires knowledge of the in situ stresses and characteristics of fault zones, including burial depth and fault dip. Both the magnitude and orientation of in situ stresses relative to the fault orientation are significant for fault reactivation analysis and geomechanical modeling (Zoback and Gorelick 2012). The level of risk for each event varies between sites, depending on the characteristic of burial depth and fault dip (Shapiro et al. 2011).

The slippage on the fault surface is influenced by many factors. Some factors are intrinsic to the surface (such as the Young's moduli, Poisson's ratios, permeability, and porosities in the rock layers), and other factors (such as the fault burial depth, fault dip, and distance between the injection well and fault surface) are controllable during site selection and injection well placement. Specifically, fault instability can be effectively avoided through risk management of these three controllable factors. Substantially reduced levels of risk associated with fluid injection can be achieved by placing CO_2 injection wells in optimal locations. Kumar (2007) applied an optimization approach based on the conjugate gradient method and used a commercial simulator as a black box for the calculation of numerical gradients to minimize structurally trapped CO_2 in heterogeneous two-dimensional (2D) models. Nghiem et al. (2010) considered the optimal location and operating strategies for a water injection well situated above a CO_2 injection well in a three-dimensional (3D) saline aquifer model. Cameron and Durlofsky (2012) applied a Hooke–Jeeves direct search algorithm to minimize the mobile fraction of CO_2 at the end of a 1,000-year injection and storage operation in a brine aquifer; the optimization variables included the CO_2 injection well locations and injection rate schedules as well as the timing and injection/production volumes of brine. In addition, the potential behaviors involving fluid injection for all fault orientations and dips were studied using an analytical approach (Mildren et al. 2002; Sibson 1998).

To optimize the site performance and management, guidelines include setting the acceptable level (i.e., magnitude range) and outlining the control measurements, which should be established before injection commences (Gerstenberger et al. 2013). A site performance and management system, referred to as the traffic light system, which has been proposed for enhanced geothermal systems, was introduced in this work (Bommer et al. 2006; Majer et al. 2007). With the purpose of reducing the risk of fault reactivation by optimizing well placement, we extended the previous studies in several important ways. First, rather than using analytical approaches, we applied a numerical approach to evaluate the potential magnitude of the fault slippage for a specific stress regime. Next, we focused on the geometry and structures of fault zones using comprehensive analyses of the fault burial depth, fault dip, and well location. Based on the corresponding fault behavior, we obtained a traffic light indicator diagram to indicate the risk of induced seismicity at a specific level of each factor. Furthermore, to overcome the existence of the complicated relationship between factor variations and the corresponding fault slippage and to guide well placement to effectively reduce the risk of inducing strong seismicity, we introduced a danger surface in the traffic light indicator diagram with a security threshold to distinguish the danger zone.

Methodology

Theoretical Background

Rock masses exhibit anisotropic and heterogeneous properties that are greatly dependent on the types of rock, diagenetic and geological processes, and burial depths (Jaeger et al. 2009; Zhou and Burbey 2014b). To capture the coupled fluid and geotechnical behavior of these systems, the hydromechanical coupling approach is a very powerful and practical mathematical approach (Coussy 2004). The static poroelastic field equation can be given as follows:

$$2G\varepsilon_{ij} = \sigma_{ij} - \frac{v}{1+v}\sigma_{kk}\delta_{ij} + \frac{3(v_u - v)}{B(1+v)(1+v_u)}p\delta_{ij} \quad (1)$$

$$\Delta m = \frac{3\rho_0(v_u - v)}{2GB(1+v)(1+v_u)}\left(\sigma_{kk} + \frac{3}{B}p\right) \quad (2)$$

where σ_{ij} and ε_{ij} = components of stress and strain; p = pore pressure; ρ_0 = pore-fluid density; G = shear modulus; δ_{ij} = Kronecker delta; B = Skempton's B coefficient; v_u and v = undrained and drained Poisson's ratios, respectively; and Δm = fluid mass change per unit volume (Rice and Cleary 1976).

Before the fluid has time to diffuse appreciably, the poroelastic medium is in the undrained state ($\sigma_{kk} = 3\sigma$ and $\Delta m = 0$), and the undrained pore pressure could be mathematically implied as

$p = -B\sigma$. Afterward, the pore fluids flow to regions of dilation from regions of compression, and the pore-pressure change can be implied as (Roeloffs 1996)

$$p = -\frac{2GB(1+v_u)}{3(1-2v_u)}\varepsilon_{kk} \tag{3}$$

In the fault-slip modeling, an implicit finite-element method (FEM) is used for problems involving contacts. In the standard Coulomb friction model, no fault slippage will occur when the equivalent frictional stress ($\tau_{eq} = \sqrt{\tau_1^2 + \tau_2^2}$) is less than the critical stress [$\tau_{\text{crit}} = \Psi(\sigma_n - p)$], where τ_1 and τ_2 refer to the two shear stresses on the plane. If the equivalent stress is at the critical stress, relative motion will occur, and the direction of the slip coincides with the frictional stress under an isotropic frictional condition

$$\frac{\tau_i}{\tau_{eq}} = \frac{v_i}{\sqrt{v_1^2 + v_2^2}} \tag{4}$$

where v_i = slip rate in direction i; and $\sqrt{v_1^2 + v_2^2}$ = magnitude of slip rate corresponding to equivalent stress (Zhou and Burbey 2014b).

Traffic Light System

The traffic light system is aimed at managing risks related to the fault burial depth, the fault dip, and the distance between the injection well and fault surface. The system may use two or more thresholds to define the risk of the project in terms of induced seismicity. The thresholds for the risk of inducing felt earthquakes, in terms of guiding decisions regarding the well location, were as follows:

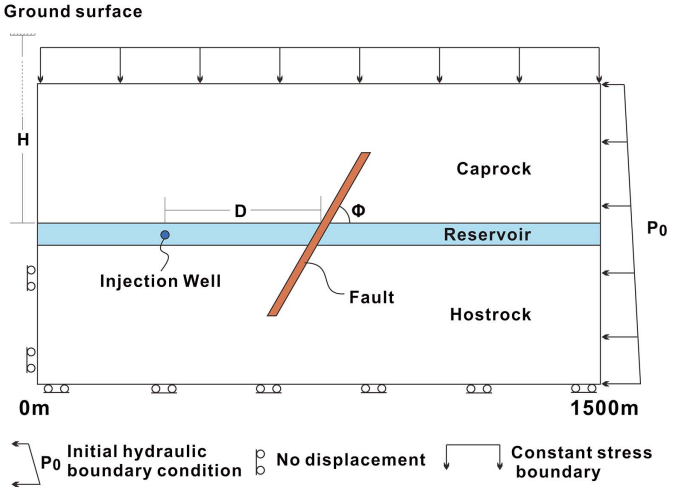

Fig. 1. Model conceptualization. H = thickness of the overburden from the reservoir to the ground surface; D = distance between the injection well and the fault; and Φ = fault dip.

Green: In the green zone, no felt seismicity is induced over the entire ranges of fault burial depth and fault dip.

Amber: In the amber zone, there is a limited magnitude of induced fault slippage at certain fault dips and at a certain depth. Pumping is permitted to proceed with caution, possibly at reduced injection pressure, and observations are intensified.

Red: In the red zone, the fault in all scenarios is at high risk of suffering induced felt seismicity. To mitigate the risk, the red zone should be avoided in well setting.

In this study, coupling of a traffic light system with numerical modeling provided a basis for quantifying the risk of seismicity beyond injection, because numerical physical modelling may provide a basis for optimal well location prior to the start of operations or before acceptable induced seismicity limits are exceeded. To thoroughly investigate the relationship between the controllable factors and the fault behavior, based on numerical simulation, we introduced a traffic light indicator diagram to evaluate the magnitude of the fault slippage, using three axes that represent the fault burial depth (H), the fault dip (Φ), and the distance between the injection well and fault surface (D).

Simulations were performed in the lower portion of a sedimentary basin simplified to a rectangle 1,500 × 800 m.

The thickness of the overburden (H) of the reservoir was set to five equal-sized levels, ranging from 800 to 3,200 m. A vertical stress existed from the weight of the overburden rock with a bulk density ρ of 2,600 kg/m^3, and the horizontal stress was scaled by a factor of 0.6 with respect to the vertical stress. The initial pore pressure was assumed to be hydrostatic. The main feature of the model was the 0-m offset fault located at the center of the model dip (Φ) from 10° to 90°, with a 20-m length along the dip and a 500-m-long fault surface. We assumed that the fault core had the same properties along the entire fault, and the hydraulic conductivity of the fault zone was assumed to be isotropic.

The boundary conditions were fixed in the lateral direction on both sides of the model, and the bottom of the model was fixed in the vertical direction (Fig. 1). The layers were considered to be elastic, whereas the faults had an elastoplastic behavior described by a Mohr–Coulomb mechanical model. The values for the material properties in Table 1 were abstracted from observations and variations observed in Shenhua carbon capture and storage (CCS) demonstration projects (Lei et al. 2008; Li et al. 2013; Pereira et al. 2014). The material properties for each material are presented in Table 1. The nephograms are presented in Fig. 2 to show the pore-pressure distribution during fluid injection.

Numerical Solution

Stability studies using constitutive relations to describe fault slippage in the laboratory have provided explanations of the depth cutoff of crustal earthquakes (Dieterich 1981; Ruina 1983). The predicted earthquake cycles involve overall features that appear to be in good agreement with the normal stress, slip rate, and slip history of strike-slip earthquakes along a fault; however, the initiation depth for the seismic activity appears to change unpredictably with small changes in the constitutive description (Tse and Rice

Table 1. Mechanical properties for each region considered in model

Stratum	Permeability (m^2)	Porosity	Young's modulus (GPa)	Poisson's ratio	Cohesion (MPa)	Friction angle (degrees)
Reservoir	1.00×10^{-11}	0.2	42	0.3	—	—
Caprock	1.00×10^{-16}	0.01	30	0.37	—	—
Host rock	1.00×10^{-16}	0.01	30	0.37	—	—
Fault	1.00×10^{-14}	0.1	10	0.3	1	14

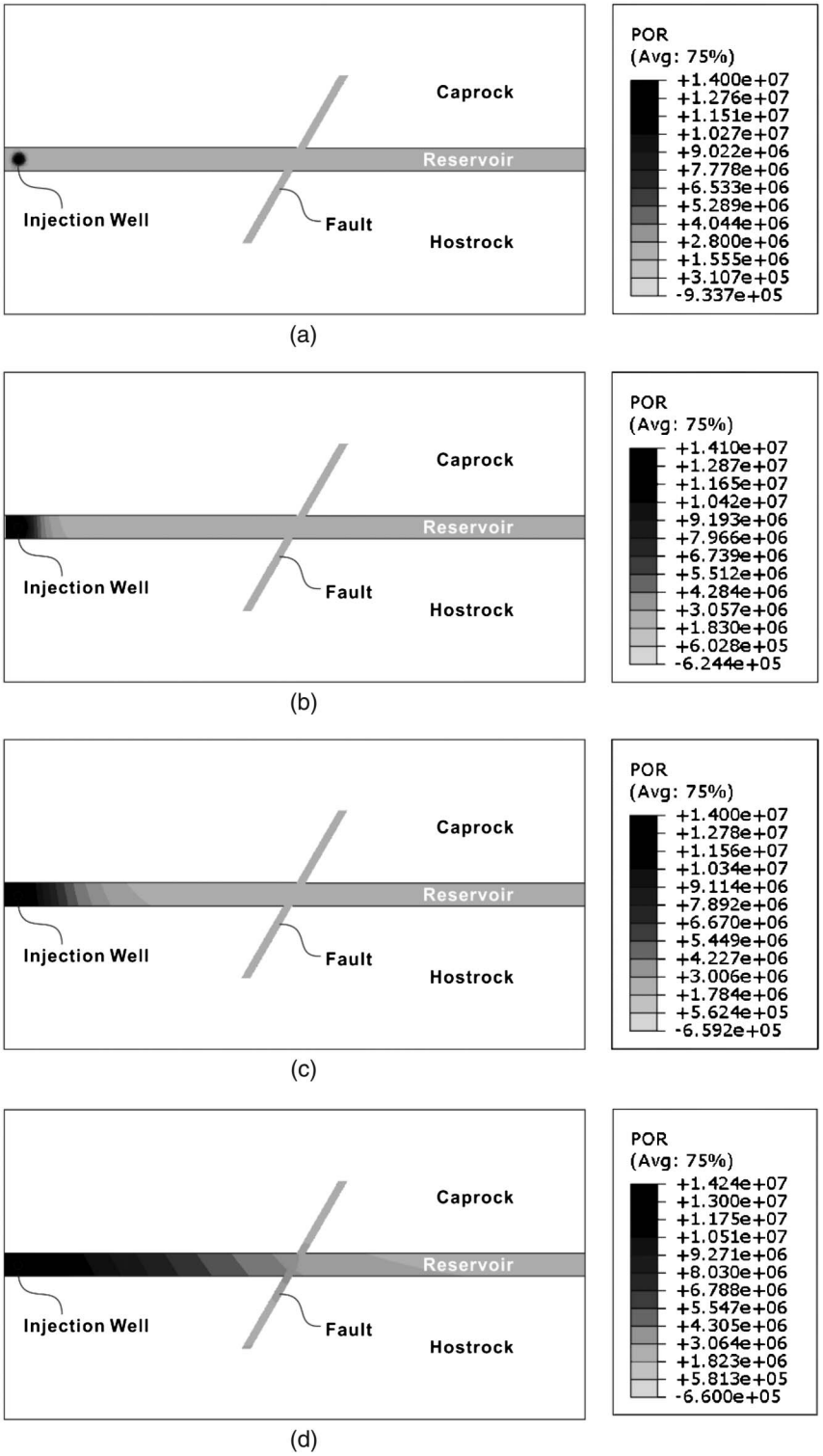

Fig. 2. Pore-pressure (Pa) distribution at different times after the start of injection: (a) $t = 1$ day; (b) $t = 1$ month; (c) $t = 1$ year; and (d) $t = 10$ year.

1986). A survey of the induced seismic responses to different geometries of fault zone structure not only showed that the seismic responses share some common features but also revealed unique characteristics for each individual case, indicating the complexity of such problems (Evans et al. 2012).

In the process of reservoir development, one wishes to drill wells at the optimal locations because of the advantages of construction convenience and long-term safe storage. Computational optimization techniques were applied to well placement by many researchers (Cameron and Durlofsky 2012; Kumar 2007; Zhang et al. 2010). The goal of the present study was to determine the well location that minimizes the magnitude of the induced seismicity. The fault behavior obviously is very site-specific and depends on the local in situ stress conditions and mechanical properties of the rock (Evans et al. 2012). To study the relationship between the controllable factors and the corresponding fault slippage, we used a traffic light detection method to describe the magnitude of induced fault slippage. First we calculated the induced fault slippage with

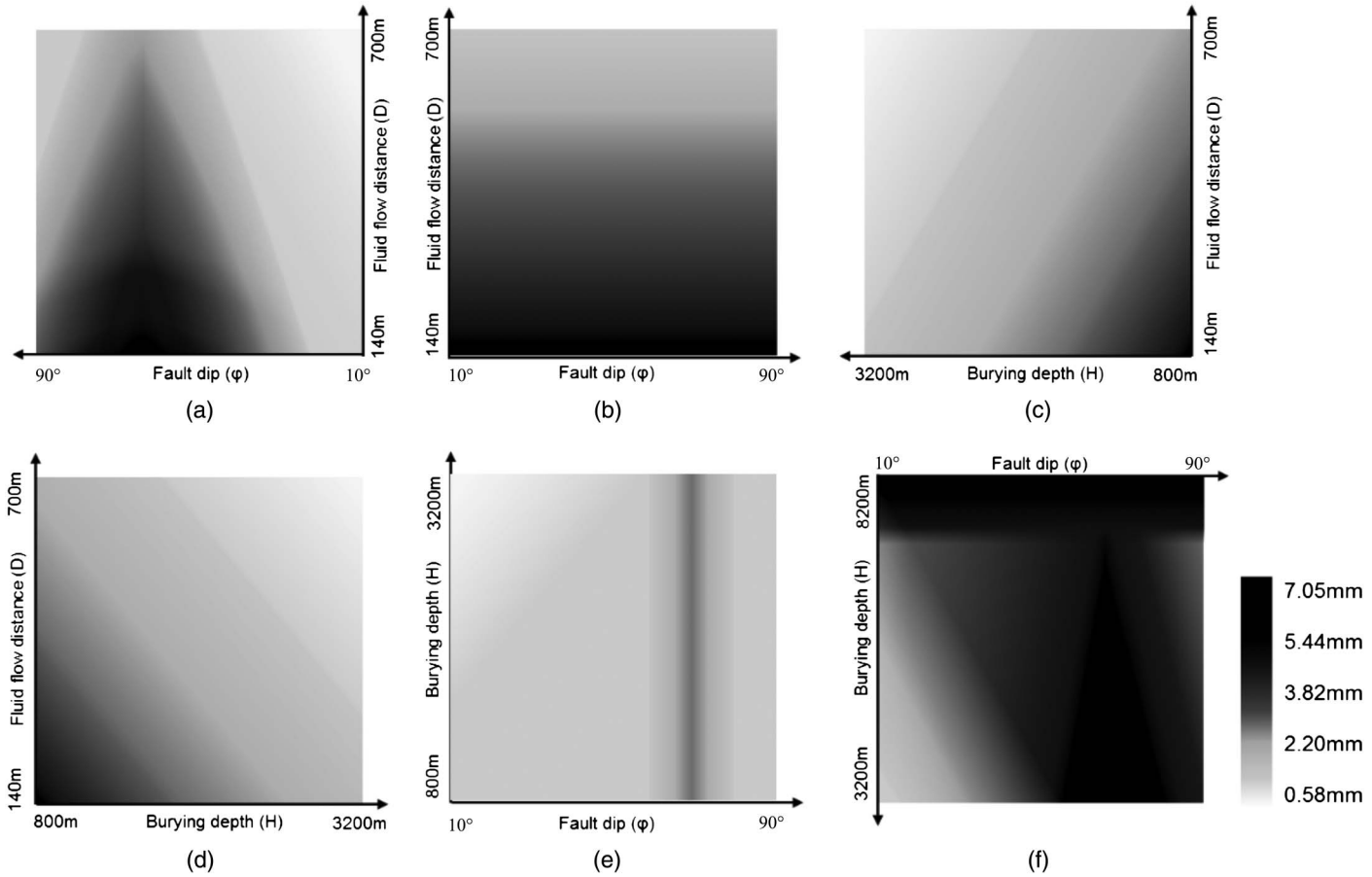

Fig. 3. Three-dimensional discrete induced fault slippage for burying depth (H) at five levels equally spaced over the range 800–3,200 m, fluid flow distance (D) at five levels equally spaced over the range 140–700 m, and fault dip (Φ) at nine levels equally spaced over the range 10°–90°: (a) front view; (b) back view; (c) left-side view; (d) right-side view; (e) top view; and (f) bottom view.

the 2D numerical model at every specified level of H (800, 1,400, 2,000, 2,600, and 3,200 m), D (140, 280, 350, 420, 560, and 700 m), and Φ (10°, 20°, 30°, 40°, 50°, 60°, 70°, 80°, and 90°), and the discrete induced fault slippage value is shown in Fig. 3, with the shading indicating the magnitude of fault slippage at every specific level of each factor.

Results and Discussion

Effect of Distance between Injection Well and Fault

It is well accepted that the maximum increase in the pore pressure occurs near the injection well zone and that farther locations experience less pore-pressure increase. A lower pore pressure corresponds to a higher effective stress and a lower risk of failure (Vilarrasa et al. 2016). Fig. 4 illustrates the profiles of induced fault slippage along the 500-m fault plane in the 3,200-m reservoir, with a fault dip of 70° after 20 years of fluid injection; the induced fault slippage was influenced by different injection wells 140, 280, 420, 560, and 700 m horizontally from the fault. The induced fault slippages presented similar variation tendencies: the upper portion of the fault plane slipped downward and the lower portion of the fault plane slipped upward. Moreover, the induced fault slippage became violent at 180 and 320 m, resulting in squeezing at the middle position (near 250 m) of the fault plane, and the induced slippage here was reduced to zero. In addition, there was a clear negative correlation between the magnitude of induced slippage and the distance between the injection well and the fault (D): the maximum induced fault slippages at D of 140, 280, 420, 560, and 700 m were 0.0188, 0.0150, 0.0125, 0.0107, and 0.0093 m, respectively, and the maximal induced fault slippages here were

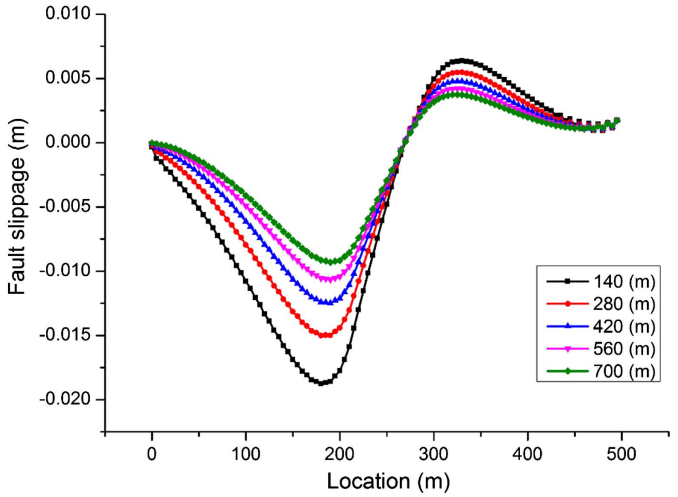

Fig. 4. Profiles of maximal induced fault slippage along the 500-m fault plane influenced by different injection wells 140, 280, 420, 560, and 700 m horizontally from the fault in the 3,200-m reservoir, with a fault dip of 70° during fluid injection.

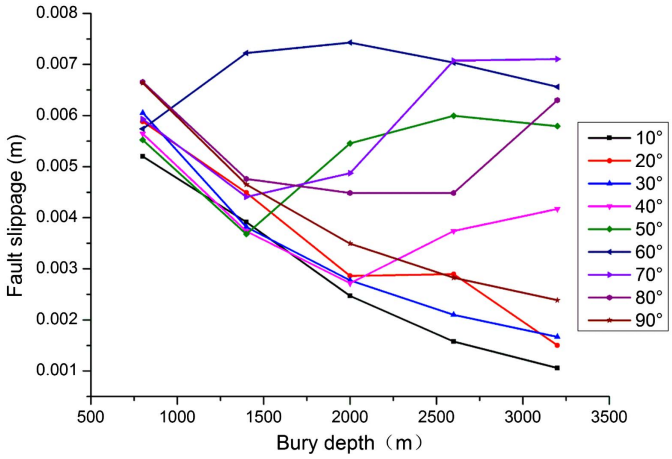

Fig. 5. Relationship between the variation of H/Φ and the corresponding maximal fault slippage when the injection well is 140 m from the fault during 20 years of fluid injection.

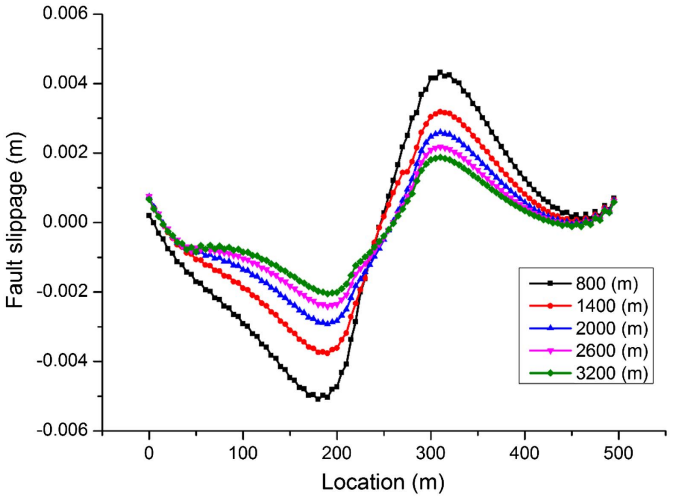

Fig. 6. Profiles of maximal induced fault slippage along the fault plane influenced by different values of H at a fault dip of 90° with the injection well 700 m from the fault.

0.0071, 0.0056, 0.0047, 0.0040, and 0.0035 m, respectively. In addition, because of the reduced pore-pressure increase at locations farther from the injection zone, this negative correlation between the magnitude of induced slippage and D was not site specific but existed at every thickness of the overburden and fault dip.

Effect of Thickness of Overburden and Fault Dip

The relationship between the variation of H/Φ and the corresponding maximal fault slippage when the injection well is 140 m from the fault during 20 years of fluid injection is presented in Fig. 5. The induced fault slippage generally decreased with depth when the fault was gentle or steep, at fault dips of 10°, 20°, 30°, and 90°. Taking 90° as an example scenario, the profiles of induced fault slippage along the fault plane influenced by different H when the injection well is 700 m from the fault are shown in Fig. 6. The induced fault slippages exhibited similar variation tendencies to that shown in Fig. 4, and a negative correlation was found between the magnitude of the induced slippage and the thickness of the overburden (H): the maximal induced fault slippages at H of 800, 1,400, 2,000, 2,600, and 3,200 m were 0.00232, 0.00164, 0.00127, 0.00104, and 0.0009 m, respectively.

At these fault dips, the induced fault slippage increased with depth below 2,200 m, and at 60°, the induced fault slippage was relatively large at all depths. The strength of the fault surface is governed by the Mohr–Coulomb yield criteria, and the fault slippage is calculated by a master-subordinate contact algorithm. The magnitude of fault slippage is significantly affected by the favorable failure angle, which is determined by the material property of the system. Because the internal friction angle was 15° in the fault, 30° in the caprock, and 40° in the sandstone reservoir, despite other influencing factors, the favorable failure angle was about 60° as calculated by the Mohr-coulomb yield criteria. Thus, the fault dip at the favorable failure angle, which was about 60°, would cause large slippages. The fault slippage includes two parts, the slippage in the caprock and in the reservoir. According to the quantification of the seismic moment presented by Hanks and Boore (1984), we adopted average fault slippage to present the mechanical response of the fault surface to fluid injection. At certain fault dips near the favorable failure angle, below 2,200 m the shear stress exceeded the reactivation threshold at larger portion on the fault plane in the caprock, and thus the slippage accounted for a greater proportion of the fault; as a result, the average fault slippage increased with depth below 2,200 m for certain fault dips near the favorable failure angle.

Danger Surface

The moment magnitude scale (M_w) is used by seismologists to measure the size of seismicity in terms of the energy released. In this model, fault slippages correspond to the coseismic phase of an earthquake, and the magnitude is based on the seismic moment (denoted M_0) of the earthquake; from the relationships presented by Hanks and Boore (1984), the quantification of the seismic moment (M_0) is equal to the rigidity of the earth (Φ) multiplied by the maximal amount of slippage in the fault (d) and the size of the area that slipped (A) (Hanks and Boore 1984). Because our simulations were conducted in a plane-strain model, a unit lateral extent for rupture (A) can be assumed. The moment magnitude (M_w) of an earthquake is given in terms of the seismic moment (M_0) of an earthquake: $M_w = (\log_{10}M_0 - 9.0)/1.5$ (Thatcher and Hanks 1973). Seismicity of $M_w > 3.0$ is defined as minor seismicity, which often can be felt by people and shaking of indoor objects can be noticeable (Richter 1935). For this reason, in this study, we used $M_w = 3.0$ as a security threshold, with a corresponding fault slippage (d) of 12 mm.

To overcome the existence of the complicated relationship between the variation of H/Φ and the corresponding fault slippage and to effectively guide well placement to reduce the risk of inducing strong seismicity, we introduced a danger surface in the traffic light indicator diagram (Fig. 4) with a security threshold of 12 mm to distinguish the danger zone. Fig. 7(a and b) display the danger surface in the 3D traffic light indicator diagram; the area underneath this black surface is defined as the danger zone that may induce damage seismicity. Figs. 7(b–d) display the top view, front view, and right-side view of the 3D diagram, respectively. The distance from the injection well to the fault (D) is the key factor [Fig. 7(a)], and three zones were developed based on their probability of inducing felt seismicity.

Green zone ($D > 350$ m): No felt seismicity is induced over the entire ranges of fault burial depth and the fault dip.

Amber zone ($230 < D < 350$ m): Only a limited magnitude of induced fault slippage occurs at certain fault dips ($\Phi = 10°$, 20°, 30°, and 90°), and most cases are safe for operation of fluid

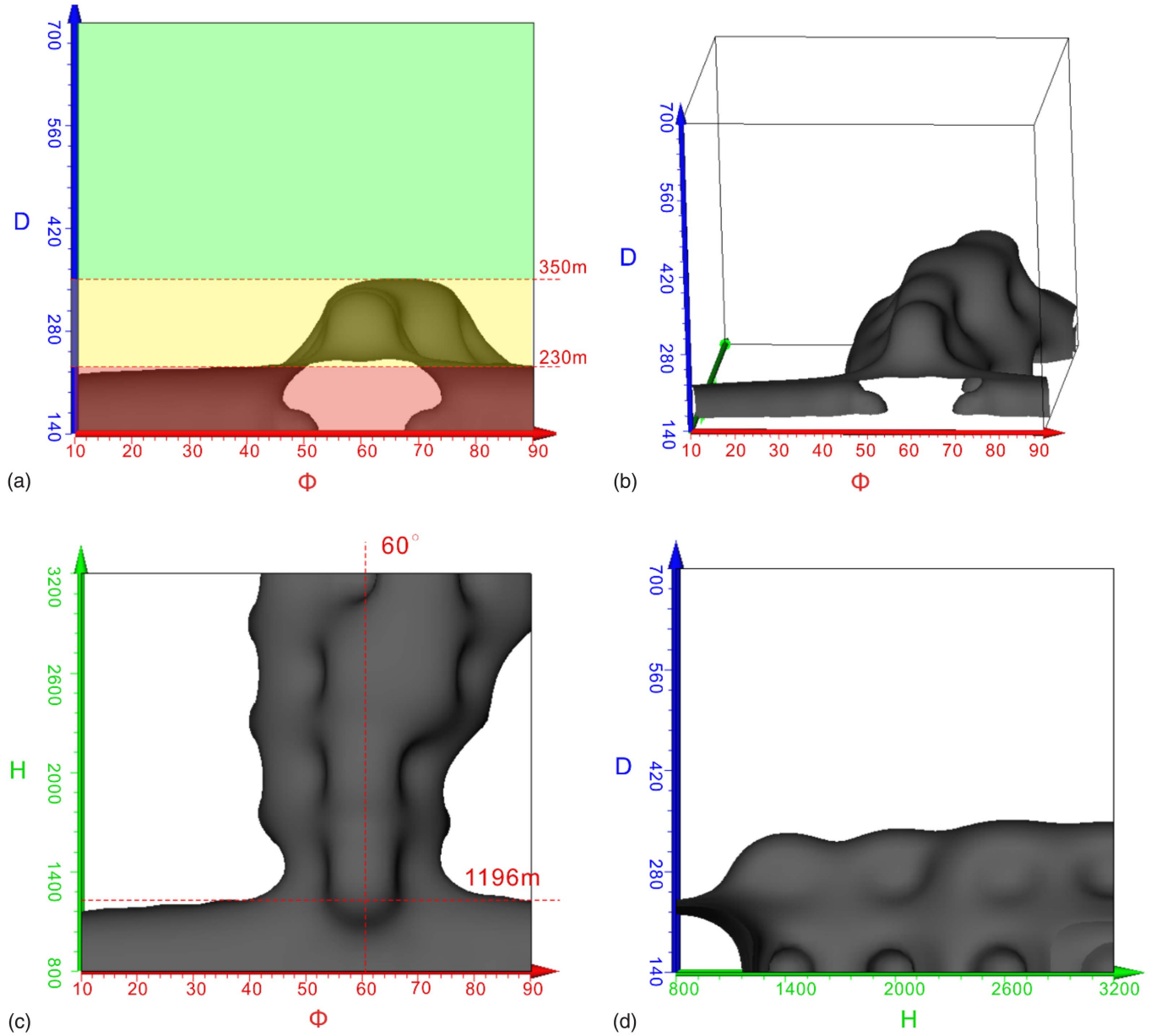

Fig. 7. (a) Traffic light indicator diagram; (b) danger surface; (c) front view of the 3D diagram; and (d) right-side view of the 3D diagram.

injection at a certain depth ($H > 1{,}196$ m). At some fault dips ($\Phi = 40°$, 70°, and 80°), the induced fault slippage increases with depth below 1,196 m (Fig. 5), and at 60°, the induced fault slippage is relatively large at all depths [Fig. 7(b)]. Pumping is permitted to proceed with caution, possibly at reduced injection pressure, and observations are intensified.

Red zone ($D < 230$ m): The fluid injection near a fault at shallow depth ($H < 1{,}196$ m) for all fault dips is at high risk of suffering induced felt seismicity [Figs. 7(a and c)].

Conclusions

Underground fluid injection activities could induce fault-slip that results in devastating damage to caprock stability. In this work, with the purpose of reducing the risk of fault reactivation by optimizing well placement, we focused on the geometry and structures of the fault zones based on comprehensive analyses of the fault burial depth, fault dip, and well location, and applied a numerical approach to evaluate the potential magnitude of the fault slippage for a specific stress regime. Based on the relationships of D, H, and Φ (where D is the distance between the fault and the injection well, H is the burial depth of the target reservoir, and Φ is the fault dip) with the corresponding fault behavior, we obtained a traffic light indicator diagram and a danger surface to indicate the risk of induced seismicity at a specific level of each factor. The following conclusions can be drawn based on the investigation:

1. Because of the reduced pore-pressure increase at locations farther from the injection zone, the negative correlation between the magnitude of the induced slippage and the distance between the fault and the injection well (D) is not site-specific but exists at every thickness of the overburden and fault dip.
2. The induced fault slippage events had similar tendencies (with the upper portion of the fault plane slipping downward and the lower portion of the fault plane slipping upward) and became

violent at 180 and 320 m, resulting in squeezing at the middle position of the fault plane; the induced slippage here was reduced to zero.
3. The induced fault slippage generally decreases with depth when the fault is gentle or steep. The fault dip at the favorable failure angle, which was about 60°, would cause large slippages. At certain fault dips near the favorable failure angle, below 2,200 m the shear stress exceeded the reactivation threshold over a larger portion of the fault plane in the caprock, and the average fault slippage increased with depth below 2,200 m for certain fault dips near the favorable failure angle.
4. The distance from the injection well to the fault (D) is the key factor to avoid felt seismicity [Fig. 7(a)]. In the traffic light indicator diagram, no felt seismicity would be induced in the green zone, and in the amber zone, felt seismicity is unlikely at certain fault dips (10°, 20°, 30°, and 90°). In the red zone, the risk is high for induced felt seismicity for all fault dips.

Data Availability Statement

All data, models, and code generated or used during this study may be obtained upon request.

Acknowledgments

This work was supported by the National Natural Science Foundation of China (NSFC) under Grant Nos. 41872210, 41274111, and 51809220; the Open Research Fund of State of Key Laboratory of Geomechanics and Geotechnical Engineering under Grant No. Z017008; and the Young Scholars Development Fund of SWPU under Grant No. 201699010097. We also thank the financial support provided by the China National Key Technology R&D Program (Grant No. 2012BAC24B05), the United Fund Project of National Natural Science Foundation of China (Grant No. U1262209), and the National Science and Technology Major Project of the Ministry of Science and Technology of China "Development of Large Oil and Gas Field and Coalbed Methane" (Grant No. 2016ZX05044-004-001).

References

Bommer, J. J., S. Oates, J. M. Cepeda, C. Lindholm, J. Bird, R. Torres, G. Marroquín, and J. Rivas. 2006. "Control of hazard due to seismicity induced by a hot fractured rock geothermal project." *Eng. Geol.* 83 (4): 287–306. https://doi.org/10.1016/j.enggeo.2005.11.002.

Cameron, D. A., and L. J. Durlofsky. 2012. "Optimization of well placement, CO_2 injection rates, and brine cycling for geological carbon sequestration." *Int. J. Greenhouse Gas Control* 10 (Sep): 100–112. https://doi.org/10.1016/j.ijggc.2012.06.003.

Cappa, F., and J. Rutqvist. 2012. "Seismic rupture and ground accelerations induced by CO_2 injection in the shallow crust." *Geophys. J. Int.* 190 (3): 1784–1789. https://doi.org/10.1111/j.1365-246X.2012.05606.x.

Childs, C., J. Watterson, and J. Walsh. 1996. "A model for the structure and development of fault zones." *J. Geol. Soc.* 153 (3): 337–340. https://doi.org/10.1144/gsjgs.153.3.0337.

Coussy, O. 2004. *Poromechanics*. New York: Wiley.

Dieterich, J. H. 1981. "Constitutive properties of faults with simulated gouge." In *Mechanical behavior of crustal rocks: The Handin volume*, 103–120. Washington, DC: American Geophysical Union.

Ellsworth, W. 2013. "Injection-induced earthquakes." *Science* 341 (6142): 1225942. https://doi.org/10.1126/science.1225942.

Evans, K. F., A. Zappone, T. Kraft, N. Deichmann, and F. Moia. 2012. "A survey of the induced seismic responses to fluid injection in geothermal and CO_2 reservoirs in Europe." *Geothermics* 41 (Jan): 30–54. https://doi.org/10.1016/j.geothermics.2011.08.002.

Gerstenberger, M., A. Nicol, C. Bromley, and R. Carne. 2013. *Induced seismicity and its implications for* CO_2 *storage risk.* Cheltenham, UK: IEA Greenhouse Gas R&D Program.

Gutierrez, M., L. Øino, and R. Nygård. 2000. "Stress-dependent permeability of a de-mineralised fracture in shale." *Mar. Pet. Geol.* 17 (8): 895–907. https://doi.org/10.1016/S0264-8172(00)00027-1.

Hanks, T. C., and D. M. Boore. 1984. "Moment-magnitude relations in theory and practice." *J. Geophys. Res.: Solid Earth* 89 (B7): 6229–6235. https://doi.org/10.1029/JB089iB07p06229.

Häring, M., U. Schanz, F. Ladner, and B. Dyer. 2008. "Characterisation of the Basel 1 enhanced geothermal system." *Geothermics* 37 (5): 469–495. https://doi.org/10.1016/j.geothermics.2008.06.002.

Holloway, S. 1997. "An overview of the underground disposal of carbon dioxide." Supplement, *Energy Convers. Manage.* 38 (S1): S193–S198. https://doi.org/10.1016/S0196-8904(96)00268-3.

Horton, S. 2012. "Disposal of hydrofracking waste fluid by injection into subsurface aquifers triggers earthquake swarm in central Arkansas with potential for damaging earthquake." *Seismol. Res. Lett.* 83 (2): 250–260. https://doi.org/10.1785/gssrl.83.2.250.

IEA (International Energy Agency). 2006. *Energy technology perspectives 2006: Scenarios and strategies to 2050: In support of the G8 plan of action*. Paris: OECD/IEA (Organisation for Economic Co-Operation and Development/International Energy Agency).

IPCC (Intergovernmental Panel on Climate Change). 2005. "IPCC special report on carbon dioxide capture and storage." In *Proc., Working Group III of the Intergovernmental Panel on Climate Change Intergovernmental Panel on Climate Change*. Cambridge, UK: Cambridge University Press.

Jaeger, J. C., N. G. Cook, and R. Zimmerman. 2009. *Fundamentals of rock mechanics*. New York: Wiley.

Koestler, A. G., and A. G. Milnes. 1992. "The importance of structural reservoir characterization and reservoir mechanics for enhanced oil recovery." In *Proc., 1st Conf. on Geology of the Arab World*, edited by A. Sadek, 87–109. Giza, Egypt: Cairo Univ.

Kumar, D. 2007. *Optimization of well settings to maximize residually trapped* CO_2 *in geologic carbon sequestration*. Stanford, CA: Stanford Univ.

Langhi, L., Y. Zhang, A. Gartrell, J. Underschultz, and D. Dewhurst. 2010. "Evaluating hydrocarbon trap integrity during fault reactivation using geomechanical three-dimensional modeling: An example from the Timor Sea, Australia." *AAPG Bull.* 94 (4): 567–591. https://doi.org/10.1306/10130909046.

Lei, X., G. Yu, S. Ma, X. Wen, and Q. Wang. 2008. "Earthquakes induced by water injection at ~3 km depth within the Rongchang gas field, Chongqing, China." *J. Geophys. Res.: Solid Earth* 113 (B10): B10310. https://doi.org/10.1029/2008JB005604.

Li, Q., G. Liu, X. Liu, and X. Li. 2013. "Application of a health, safety, and environmental screening and ranking framework to the Shenhua CCS project." *Int. J. Greenhouse Gas Control* 17 (Sep): 504–514. https://doi.org/10.1016/j.ijggc.2013.06.005.

Li, Q., Z. S. Wu, Y. L. Bai, X. C. Yin, and X. C. Li. 2006. "Thermo-hydro-mechanical modeling of CO_2 sequestration system around fault environment." *Pure Appl. Geophys.* 163 (11–12): 2585–2593. https://doi.org/10.1007/s00024-006-0141-z.

Li, Q., Z. S. Wu, and X. C. Li. 2004. "Stability evaluation of fault activity induced by CO_2 injection into deep saline aquifers." *J. Appl. Mech. JSCE* 7 (2): 883–890. https://doi.org/10.2208/journalam.7.883.

Luther, A., G. Axen, and J. Selverstone. 2013. "Particle-size distributions of low-angle normal fault breccias: Implications for slip mechanisms on weak faults." *J. Struct. Geol.* 55 (Oct): 50–61. https://doi.org/10.1016/j.jsg.2013.07.009.

Majer, E. L., R. Baria, M. Stark, S. Oates, J. Bommer, B. Smith, and H. Asanuma. 2007. "Induced seismicity associated with enhanced geothermal systems." *Geothermics* 36 (3): 185–222. https://doi.org/10.1016/j.geothermics.2007.03.003.

Mazzoldi, A., A. P. Rinaldi, A. Borgia, and J. Rutqvist. 2012. "Induced seismicity within geological carbon sequestration projects: Maximum earthquake magnitude and leakage potential from undetected faults."

Int. J. Greenhouse Gas Control 10 (Sep): 434–442. https://doi.org/10.1016/j.ijggc.2012.07.012.
Mildren, S. D., R. R. Hillis, and J. Kaldi. 2002. "Calibrating predictions of fault seal reactivation in the Timor Sea." *APPEA J.* 42 (1): 187–202. https://doi.org/10.1071/AJ01011.
Mitchell, T., and D. Faulkner. 2009. "The nature and origin of off-fault damage surrounding strike-slip fault zones with a wide range of displacements: A field study from the Atacama fault system, northern Chile." *J. Struct. Geol.* 31 (8): 802–816. https://doi.org/10.1016/j.jsg.2009.05.002.
Murphy, S., G. S. O'Brien, J. McCloskey, C. J. Bean, and S. Nalbant. 2013. "Modelling fluid induced seismicity on a nearby active fault." *Geophys. J. Int.* 194 (3): 1613–1624. https://doi.org/10.1093/gji/ggt174.
Nghiem, L., V. Shrivastava, B. Kohse, M. Hassam, and C. Yang. 2010. "Simulation and optimization of trapping processes for CO_2 storage in saline aquifers." *J. Can. Pet. Technol.* 49 (8): 15–22. https://doi.org/10.2118/139429-PA.
Pereira, L. C., L. J. N. Guimarães, B. Horowitz, and M. Sánchez. 2014. "Coupled hydro-mechanical fault reactivation analysis incorporating evidence theory for uncertainty quantification." *Comput. Geotech.* 56 (Mar): 202–215. https://doi.org/10.1016/j.compgeo.2013.12.007.
Réveillère, A., J. Rohmer, and J.-C. Manceau. 2012. "Hydraulic barrier design and applicability for managing the risk of CO_2 leakage from deep saline aquifers." *Int. J. Greenhouse Gas Control* 9 (Jul): 62–71. https://doi.org/10.1016/j.ijggc.2012.02.016.
Rice, J. R., and M. P. Cleary. 1976. "Some basic stress diffusion solutions for fluid-saturated elastic porous media with compressible constituents." *Rev. Geophys. Space Phys.* 14 (2): 227–241. https://doi.org/10.1029/RG014i002p00227.
Rice, J. R., and J. W. Rudnicki. 1979. "Earthquake precursory effects due to pore fluid stabilization of a weakening fault zone." *J. Geophys. Res* 84 (B5): 2177–2193. https://doi.org/10.1029/JB084iB05p02177.
Richter, C. F. 1935. "An instrumental earthquake magnitude scale." *Bull. Seismol. Soc. Am.* 25 (1): 1–32.
Roeloffs, E. 1996. "Poroelastic techniques in the study of earthquake-related hydrologic phenomena." *Adv. Geophys.* 37: 135–195. https://doi.org/10.1016/S0065-2687(08)60270-8.
Rohmer, J., C. Allanic, and B. Bourgine. 2014. "Improving our knowledge on the hydro-chemo-mechanical behaviour of fault zones in the context of CO_2 geological storage." *Energy Procedia* 63: 3371–3378. https://doi.org/10.1016/j.egypro.2014.11.366.
Ruina, A. 1983. "Slip instability and state variable friction laws." *J. Geophys. Res.: Solid Earth* 88 (B12): 10359–10370. https://doi.org/10.1029/JB088iB12p10359.
Rutqvist, J., J. Birkholzer, F. Cappa, and C.-F. Tsang. 2007. "Estimating maximum sustainable injection pressure during geological sequestration of CO_2 using coupled fluid flow and geomechanical fault-slip analysis." *Energy Convers. Manage.* 48 (6): 1798–1807. https://doi.org/10.1016/j.enconman.2007.01.021.
Rutqvist, J., A. P. Rinaldi, F. Cappa, and G. J. Moridis. 2013. "Modeling of fault reactivation and induced seismicity during hydraulic fracturing of shale-gas reservoirs." *J. Pet. Sci. Eng.* 107 (Jul): 31–44. https://doi.org/10.1016/j.petrol.2013.04.023.
Rutqvist, J., A. P. Rinaldi, F. Cappa, and G. J. Moridis. 2015. "Modeling of fault activation and seismicity by injection directly into a fault zone associated with hydraulic fracturing of shale-gas reservoirs." *J. Pet. Sci. Eng.* 127 (Mar): 377–386. https://doi.org/10.1016/j.petrol.2015.01.019.
Sabetamal, H., J. P. Carter, and S. W. Sloan. 2018. "Pore pressure response to dynamically installed penetrometers." *Int. J. Geomech.* 18 (7): 04018061. https://doi.org/10.1061/(ASCE)GM.1943-5622.0001171.
Shapiro, S. A., O. S. Krüger, C. Dinske, and C. Langenbruch. 2011. "Magnitudes of induced earthquakes and geometric scales of fluid-stimulated rock volumes." *Geophysics* 76 (6): WC55–WC63. https://doi.org/10.1190/geo2010-0349.1.
Shukla, R., P. G. Ranjith, S. K. Choi, and A. Haque. 2011. "Study of caprock integrity in geosequestration of carbon dioxide." *Int. J. Geomech.* 11 (4): 294–301. https://doi.org/10.1061/(ASCE)GM.1943-5622.0000015.
Sibson, R. H. 1998. "Brittle failure mode plots for compressional and extensional tectonic regimes." *J. Struct. Geol.* 20 (5): 655–660. https://doi.org/10.1016/S0191-8141(98)00116-3.
Sylvester, A. G. 1988. "Strike-slip faults." *Geol. Soc. Am. Bull.* 100 (11): 1666–1703. https://doi.org/10.1130/0016-7606(1988)100<1666:SSF>2.3.CO;2.
Thatcher, W., and T. C. Hanks. 1973. "Source parameters of southern California earthquakes." *J. Geophys. Res.* 78 (35): 8547–8576. https://doi.org/10.1029/JB078i035p08547.
Tse, S. T., and J. R. Rice. 1986. "Crustal earthquake instability in relation to the depth variation of frictional slip properties." *J. Geophys. Res.: Solid Earth* 91 (B9): 9452–9472. https://doi.org/10.1029/JB091iB09p09452.
Vidal-Gilbert, S., J.-F. Nauroy, and E. Brosse. 2009. "3D geomechanical modelling for CO_2 geologic storage in the Dogger carbonates of the Paris Basin." *Int. J. Greenhouse Gas Control* 3 (3): 288–299. https://doi.org/10.1016/j.ijggc.2008.10.004.
Vilarrasa, V., R. Makhnenko, and S. Gheibi. 2016. "Geomechanical analysis of the influence of CO_2 injection location on fault stability." *J. Rock Mech. Geotech. Eng.* 8 (6): 805–818. https://doi.org/10.1016/j.jrmge.2016.06.006.
Vishal, V., N. Jain, and T. N. Singh. 2015. "Three dimensional modelling of propagation of hydraulic fractures in shale at different injection pressures." *Sustainable. Environ. Res.* 25 (4): 217–225.
Wang, J. G., Y. Ju, F. Gao, and J. Liu. 2016. "A simple approach for the estimation of CO_2 penetration depth into a caprock layer." *J. Rock Mech. Geotech. Eng.* 8 (1): 75–86. https://doi.org/10.1016/j.jrmge.2015.10.002.
Yin, Q., H. Jing, H. Su, and H. Zhao. 2018. "Experimental study on mechanical properties and anchorage performances of rock mass in the fault fracture zone." *Int. J. Geomech.* 18 (7): 04018067. https://doi.org/10.1061/(ASCE)GM.1943-5622.0001187.
Zhang, K., G. Li, A. C. Reynolds, J. Yao, and L. Zhang. 2010. "Optimal well placement using an adjoint gradient." *J. Pet. Sci. Eng.* 73 (3–4): 220–226. https://doi.org/10.1016/j.petrol.2010.07.002.
Zhou, X., and T. J. Burbey. 2014a. "Deformation characteristics of a clayey interbed during fluid injection." *Eng. Geol.* 183 (Dec): 185–192. https://doi.org/10.1016/j.enggeo.2014.10.001.
Zhou, X., and T. J. Burbey. 2014b. "Pore-pressure response to sudden fault slip for three typical faulting regimes." *Bull. Seismol. Soc. Am.* 104 (2): 793–808. https://doi.org/10.1785/0120130139.
Zhu, Q., D. Zuo, S. Zhang, Y. Zhang, Y. Wang, and L. Wang. 2015. "Simulation of geomechanical responses of reservoirs induced by CO_2 multilayer injection in the Shenhua CCS project, China." *Int. J. Greenhouse Gas Control* 42 (Nov): 405–414. https://doi.org/10.1016/j.ijggc.2015.08.017.
Zoback, M. D., and S. M. Gorelick. 2012. "Earthquake triggering and large-scale geologic storage of carbon dioxide." *Proc. Natl. Acad. Sci. U.S.A.* 109 (26): 10164–10168. https://doi.org/10.1073/pnas.1202473109.